

Structural characteristics and catalytic performance of alumina-supported nanosized ceria–lanthana solid solutions†

Lakshmi Katta,^a Gode Thrimurthulu,^a Benjaram M. Reddy,^{*a} Martin Muhler^b and Wolfgang Grünert^b

Received 9th August 2011, Accepted 10th September 2011

DOI: 10.1039/c1cy00312g

Alumina-supported nanosized ceria–lanthana solid solutions ($\text{CeO}_2\text{--La}_2\text{O}_3/\text{Al}_2\text{O}_3$ (CLA) = 80 : 20 : 100 mol% based on oxides) were synthesized by a modified deposition coprecipitation method from ultra-high dilute aqueous solutions. The synthesized materials were subjected to various calcination temperatures from 773 to 1073 K to understand the surface structure and the thermal stability. Structural and redox properties were deeply investigated by different characterization techniques, namely, X-ray diffraction (XRD), Raman spectroscopy (RS), transmission electron microscopy (TEM), UV-visible diffuse reflectance spectroscopy (UV-vis DRS), X-ray photoelectron spectroscopy (XPS), temperature programmed reduction (H_2 -TPR), and Brunauer–Emmett–Teller (BET) surface area. The catalytic efficiency was evaluated for CO oxidation at normal atmospheric pressure. BET surface area measurements revealed that synthesized samples exhibit reasonably high specific surface area. As revealed by XRD measurements, samples maintain structural integrity up to 1073 K without any disproportionation of phases. XPS results suggested that there is no significant change in the Ce^{3+} amount during thermal treatments due to the absence of undesirable cerium aluminate formation. A significant number of oxygen vacancies were confirmed from Raman and UV-vis DRS measurements. The CLA 773 sample exhibited superior CO oxidation activity. The better activity of the catalyst was proved to be due to a high dispersion in the form of nanosized ceria–lanthana solid solutions over the alumina support, facile reduction, and a high oxygen storage capacity.

1. Introduction

Amongst many environmentally significant processes, the oxidation of CO is the subject of vivid interest. The main objective of many studies has been to design a suitable material with high catalytic activity, stability at high temperatures, and low-cost for commercial viability. Noble metals, such as Au, Pt, Pd, *etc.*, have been well recognized for superior activity for CO oxidation.¹ However, some serious limitations such as high cost, limited availability, and sensitivity to carbon poisoning have stimulated an extensive search for alternatives to these metal catalysts.² Non-stoichiometric oxide nanomaterials such as ceria ($\text{CeO}_{2-\delta}$) have emerged as one of the most important and perpetual constituents in many areas of chemistry, physics, and materials science.^{3–5} Recently, ceria nanoparticles have also received unprecedented attention for

various biomedical applications (for instance, they increase brain cell longevity and prevent reactive oxygen species mediated cell damage in animals) owing to their nontoxic nature and excellent biocompatibility. The use of ceria in the domain of environmental catalysis is due to its superior chemical and physical stability, and a large number of oxygen vacancies (involving facile $\text{Ce}^{4+}/\text{Ce}^{3+}$ redox chemistry) and their mobility, which are the main characteristic features of the fluorite-type oxides.^{6–8} Under elevated reaction conditions fluorite-type structure of ceria fairly retains its structural integrity, however, the monotonous aspect of ceria is significantly influenced by thermal aging: the consequences provoke its modification. Attempts to amplify the desired properties of ceria have been made where ceria is finely dispersed over a thermally stable and high surface area support material.^{9–13} Transition aluminas, which provide a high specific surface area, adequate porosity, and exhibit good mechanical and thermal properties, are therefore commonly used as supports for catalytically active phases. Hence, dispersion of ceria over alumina would allow improving the redox performance of ceria. However, after dispersion the intimate contact between the ceria and the alumina certainly facilitates the formation of CeAlO_3 which is generally expected to adversely affect the oxygen

^a *Inorganic and Physical Chemistry, Indian Institute of Chemical Technology, Uppal Road, Hyderabad-500607, India.*

E-mail: bmreddy@iict.res.in, mreddyb@yahoo.com;

Fax: +91 40 2716 0921; Tel: +91 40 27191714

^b *Laboratory of Industrial Chemistry, Ruhr-University Bochum, D-44780, Bochum, Germany. E-mail: w.gruenert@techem.rub.de*

† Electronic supplementary information (ESI) available: Additional characterization studies supporting the results which include TEM, XPS, and TPR measurements. See DOI: 10.1039/c1cy00312g

storage/release capacity (OSC) by fixing a single oxidation state. If the redox property of CeO_2 is maintained after high dispersion, it favours faster and more oxygen exchange. Recently, it was realized that the doping of ceria with an appropriate dopant minimizes the undesired interaction between alumina and ceria. Hence, various alumina supported homo- or hetero-valent ions doped ceria have come under intense scrutiny and their ability to enhance the catalytic activity has been thoroughly investigated.^{9,14–16} Amongst many transition and rare earth ions, La_2O_3 is of considerable interest mainly due to its two active roles: (i) addition of La^{3+} ions to ceria leads to the formation of $\text{Ce}_x\text{La}_{1-x}\text{O}_{2-\delta}$ solid solution where charge neutrality is ensured by a vacancy compensation mechanism, and (ii) La^{3+} as a promoter is able to stabilize phase transition of alumina by the formation of LaAlO_3 or by a two-dimensional La–Al compound coating the support; hence it prompted a renewed interest.^{17–21} Recently, some investigations were also made on ceria, lanthana, and alumina combination catalysts and suggested a competition between these two different environments ($\text{Ce}_{1-x}\text{La}_x\text{O}_{2-\delta}$ solid solution and of the perovskite-like LaAlO_3 compound) in hosting lanthanum.¹⁸ However, important aspects such as change in structural and redox properties, and how lanthanum hampers the interaction between ceria and alumina remained uncertain. Based on the aforementioned background, the present investigation was undertaken with an aim to uncover the effect of La on the behaviour of alumina supported ceria by employing various characterization techniques. In the present investigation, the formation of $\text{Ce}_x\text{La}_{1-x}\text{O}_{2-\delta}$ solid solutions which induces prominent oxygen vacancies for the oxidation reaction, and the role of La in reducing the undesirable Ce–Al interaction were also verified.

Accordingly, ceria–lanthana/alumina (CLA) solid solutions were synthesized by employing a facile deposition coprecipitation method which is industrially economical and environmentally friendly. Characterization of the synthesized materials was achieved by various techniques, namely, Brunauer–Emmett–Teller (BET) surface area, X-ray diffraction (XRD), Raman spectroscopy (RS), transmission electron microscopy (TEM), UV-vis diffuse reflectance spectroscopy (UV-vis DRS), X-ray photoelectron spectroscopy (XPS), and temperature programmed reduction (H_2 -TPR). The catalytic efficiency was evaluated for CO oxidation reaction. The improved CO activity results of the CLA solid solutions were compared with ceria–lanthana (CL), ceria/alumina (CA), and ceria–zirconia/alumina (CZA) reference materials.

2. Experimental section

2.1 Catalyst preparation

The ceria–lanthana/alumina ($\text{Al}_2\text{O}_3:\text{CeO}_2:\text{La}_2\text{O}_3 = 100:80:20$ mol% based on oxides) sample was prepared by adopting a deposition coprecipitation method from ultra-high dilute aqueous solutions. The precursors used in the synthesis were $\text{Ce}(\text{NO}_3)_3 \cdot 6\text{H}_2\text{O}$ (Aldrich, AR grade), $\text{La}(\text{NO}_3)_3 \cdot 6\text{H}_2\text{O}$ (Aldrich, AR grade), and finely powdered $\gamma\text{-Al}_2\text{O}_3$ (Harshaw). At first, a specified quantity of the finely powdered alumina was dispersed in 2000 mL deionized water and stirred for 2 h. The requisite

amounts of cerium nitrate and lanthanum nitrate were dissolved separately in 2000 mL deionized water and mixed together. Under stirring conditions, mixed nitrate solutions and the dispersed alumina solution were thoroughly mixed. The stirring was continued for another 1 h. After complete mixing, aqueous NH_3 solution was added drop-wise under vigorous stirring until the pH of the solution reached ~ 8.5 . Following the precipitation, the obtained precipitate was filtered off, washed several times with deionized water until free from anion impurities, oven-dried at 393 K for 12 h, crushed using an agate mortar to obtain the powders, and calcined at 773 K for 5 h at a heating rate of 5 K min^{-1} in air atmosphere. Subsequently, some portions of the finished catalyst were further calcined at 873, 973, and 1073 K, respectively, for 5 h using the same heating ramp.

2.2 Catalyst characterization

2.2.1 X-Ray diffraction. Powder XRD patterns were collected on a Rigaku Multiflex instrument equipped with a nickel-filtered $\text{Cu K}\alpha$ (0.15418 nm) radiation source and a scintillation counter detector. The step size and the time per step were, respectively, fixed at 0.02° and 1 s in the range of $12^\circ \leq 2\theta \leq 80^\circ$. The mean crystallite size and lattice parameters of the supported solid solution phases were calculated using earlier reported procedures.^{22,23}

2.2.2 Raman spectra. The Raman spectra were obtained at room temperature using a LabRam HR800UV Raman spectrometer (Horiba Jobin-Yvon) fitted with a confocal microscope and a liquid-nitrogen cooled charge-coupled device (CCD) detector. Samples were excited either with 325 nm of a He–Cd laser (Melles Griot Laser) or with the emission line at 632.81 nm from an Ar^+ ion laser (Spectra Physics) which was focused on the sample under the microscope with the diameter of the analyzed spot being $\sim 1 \mu\text{m}$. The acquisition time was adjusted according to the intensity of Raman scattering.

2.2.3 BET surface area. Specific surface areas of the samples were determined by a single point BET analysis of the nitrogen adsorption isotherms at liquid- N_2 temperature (77 K) recorded on a SMART SORB-92/93 instrument *via* a thermal conductivity detector (TCD). Prior to the measurement, the sample was degassed at 393 K for 2 h to remove any residual moisture. The surface area was obtained by using the desorption data.

2.2.4 Transmission electron microscopy. The TEM-HREM studies were made on a JEM-2010 (JEOL) instrument equipped with a slow-scan CCD camera and at an accelerating voltage of 200 kV. Samples for transmission electron microscopy were prepared by crushing the materials in an agate mortar, and dispersing ultrasonically in ethyl alcohol. After dispersion, a droplet was deposited on a copper grid supporting a perforated carbon film and allowed to dry. The specimen was examined under vacuum at room temperature.

2.2.5 UV-vis diffused reflectance spectroscopy. The UV-vis DRS measurements were performed over the wavelength range of $\lambda = 200\text{--}750 \text{ nm}$ using a GBS-Cintra 10e UV-vis NIR spectrophotometer with an integration sphere diffuse reflectance attachment.

2.2.6 X-Ray photoelectron spectroscopy. The XPS analysis was performed using a Shimadzu (ESCA 3400) spectrometer. The X-ray source utilized was Mg K α (1253.6 eV) radiation. The analysis was done at room temperature, and pressures were typically in the order of less than 10^{-8} Pa. Samples were out-gassed overnight in a vacuum oven before XPS measurements. The surface atomic concentrations were determined from photoelectron peak areas using the atomic sensitivity factors. All binding energies were measured within a precision of ± 0.2 eV. The binding energies were corrected by setting the binding energy (BE) of the adventitious carbon (C 1s) peak at 284.6 eV.

2.2.7 Temperature-programmed reduction. The reducibility of the catalyst was investigated by TPR using a thermal conductivity detector (TCD) of a gas chromatograph (Shimadzu) in a conventional laboratory made apparatus. About 30 mg of sample mass was loaded in an isothermal zone of the reactor and heated at a rate of 10 K min^{-1} to 473 K in 30 mL min^{-1} helium gas, which facilitated driving away of the molecules that had been pre-adsorbed on the surface of the sample. After the sample was cooled to room temperature, the helium was switched to 5% H_2/Ar with a flow rate of 20 mL min^{-1} , and the temperature was linearly raised to 1073 K at a continuous heating ramp of 5 K min^{-1} , keeping all the parameters unchanged. The hydrogen

consumption during the reduction process was calculated by passing the effluent gas through a molecular sieve trap to remove the produced water and was analyzed by a gas chromatograph (GC) using the TCD.

2.3 Activity studies

The catalytic activity of the sample for CO oxidation reaction was studied at normal atmospheric pressure in the temperature range of 300–773 K in a fixed-bed microreactor under the temperature ramp of 5 K min^{-1} . Approximately 100 mg of the catalyst sample (250–355 μm sieve fraction) was diluted with quartz particles (1:1) of the same sieve fraction and was placed in a quartz reactor with its ends plugged with ceramic wool. The reaction temperature was measured using a thermocouple placed in the hollow part of the reactor. The following gases and gas mixtures were used (supplied by Air Liquide): argon (>99.999% purity), 9.98% CO in argon (CO purity, >99.997%; argon purity, >99.99%), and 10.2% O_2 in argon (oxygen purity, >99.995%). The total flow rates maintained by three mass flow controllers were in the range of 50–60 sccm (standard cubic centimetres per minute). The CO and CO_2 gas concentrations were measured using an Uras 14 infrared analyzer module, and the O_2 concentration was measured using a Magnos 16 analyzer (Hartmann & Braun). Prior to oxidation of CO, the catalyst was heated to 773 K in a 10.2% O_2/Ar gas mixture, using a heating ramp of 10 K min^{-1} , and kept at the final temperature for 1 h. The oxidized sample was then purged in argon to avoid gas phase reaction and cooled to the desired starting temperature. The CO/ O_2 reactant feed ratio was 1, and partial pressures of CO and O_2 were in the range of 10 mbar.

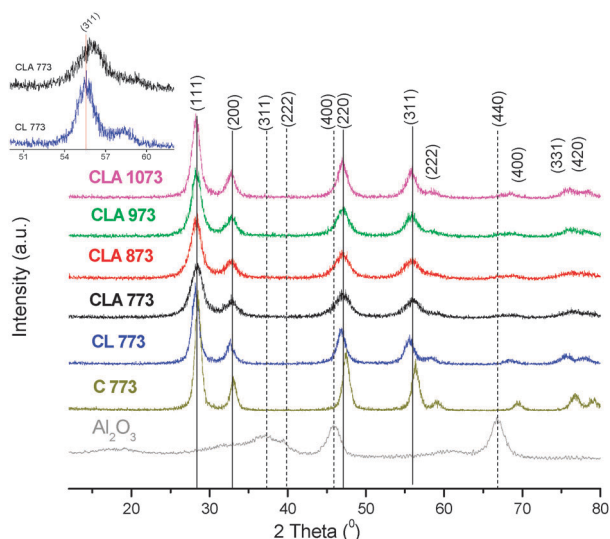


Fig. 1 Powder XRD patterns of $\gamma\text{-Al}_2\text{O}_3$, ceria (C), ceria-lanthana (CL), and alumina supported ceria-lanthana (CLA) (inset: expanded view).

Table 1 Surface area, average crystallite size, lattice parameter, and relative H_2 consumptions for ceria (C), ceria-lanthana (CL), and ceria-lanthana/alumina solid solutions (CLA) calcined at various temperatures

Sample	Surface area/ m^2 per g of sample	Crystallite size ^a /nm	Lattice parameter ^a /Å	Relative H_2 consumption per g of ceria
C 773	41	8.9	5.410	1
CL 773	66	8.3	5.488	1.04
CL 1073	40	15.6	5.492	0.82
CLA 773	108	4.6	5.461	2.14
CLA 873	90	5.3	5.462	—
CLA 973	79	6.3	5.459	—
CLA 1073	72	6.8	5.461	1.48

^a From XRD.

3. Results and discussion

3.1 Structural characterization

The powder XRD patterns of the CLA sample calcined at various temperatures are presented in Fig. 1. For reference purpose, we have also included the XRD patterns of $\gamma\text{-Al}_2\text{O}_3$, pure ceria (C), and CL samples. Crystallite size, lattice parameter, and surface area of all these samples are given in Table 1. The employed $\gamma\text{-Al}_2\text{O}_3$ sample has the specific surface area, crystallite size, and lattice parameter values of $127\text{ m}^2\text{ g}^{-1}$, 4.7 nm, and 7.926 Å, respectively. As observed from the figure, the XRD peaks of CL relative to ceria are systematically shifted to the lower angle side which is also reflected by an increase in the lattice parameter “ a ” (Table 1). A shift in the peak positions

can be explained on the basis of difference in the ionic radii of guest (La^{3+} : 0.116 nm) and host ions (Ce^{4+} : 0.097 nm).²⁴ Further, these observations indicate the formation of solid solution, tentatively formulated as $\text{Ce}_{1-x}\text{La}_x\text{O}_{2-\delta}$, signifying that charge neutrality is attained by the O-vacancy compensation mechanism.^{17,25}

Interestingly, no peaks pertaining to the $\gamma\text{-Al}_2\text{O}_3$ phase were observed in the CLA samples, which could be due to the presence of the support in an amorphous form. It is also observed that the diffraction patterns of CLA samples at all calcination temperatures show the typical peaks of the fluorite-type structure. An increase in the overall width and decrease in the intensity of peaks are also observed when alumina is used as the support. In addition, there is a decrease in the lattice parameter with reference to the unsupported CL (5.488 Å) sample which is confirmed by a small shift in the diffraction peak positions to higher Bragg angles.^{24,26} This observation is evident when (311) reflections are compared (see the inset in Fig. 1). Interestingly, with increase in the calcination temperature there is no significant change in the lattice parameter. The plausible reason for the decrease in the lattice parameter (CLA 773) could be due to a small amount of La^{3+} that may come out of the lattice and segregate at the interface, and with increase in the calcination temperature the segregated lanthanum gradually enters into the vacant octahedral sites of the alumina. Supporting this result, a few reports are also available in the open literature signifying that there is a strong interaction between La and Al.^{18,26} Therefore, we can expect the formation of a LaAlO_3 compound as a similar observation was made earlier in the literature. However, under the investigated conditions such a type of compound is not apparent from the XRD patterns, may be due to either the presence of the compound in an amorphous form or its formation in a very low amount that could be beyond the detection limit.

The crystallite sizes of the CLA samples calcined at various temperatures are calculated using the Scherrer equation by means of a line broadening method. As the calcination temperature increased, a distinct sharpening and increased intensity of the peaks are obvious owing to better crystallization. Crystallite sizes of the supported samples are lower than the unsupported samples and fall in the 4–7 nm range for 773–1073 K temperatures. A plateau in the crystallite size and stable lattice constants impart excellent dispersion of the CL on the alumina support and the alumina is able to stabilize the particle size in the nanorange.

The contribution of CL to the surface area of CLA was estimated to be $\sim 98 \text{ m}^2 \text{ g}^{-1}$ CL by assuming that the surface area of alumina is same, before and after the deposition. This increased surface area of CL in CLA compared to unsupported CL ($66 \text{ m}^2 \text{ g}^{-1}$) is due to better dispersion, which makes the active component deposited as a layer on the support surface. Representative HREM and TEM pictures of CLA samples prepared by deposition coprecipitation and calcined at 773 and 1073 K are shown in Fig. 2A and B and Fig. S1 (ESI†), respectively. The observed clear lattice fringes revealed a high degree of crystallinity that are unambiguously corresponding to CL particles with a mean diameter of around 4–6 nm having no preferential orientation and connected to each other by joint boundaries to obtain larger ensembles (inset, Fig. 2B).

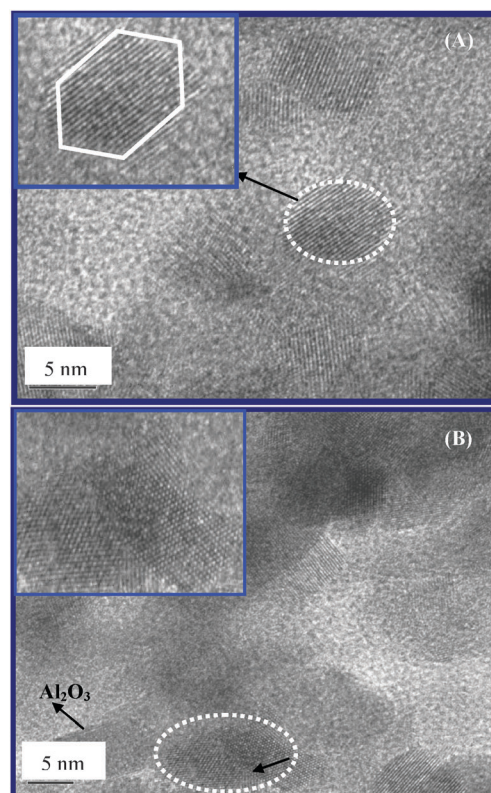


Fig. 2 HREM micrographs of (A) 773 K and (B) 1073 K calcined alumina supported ceria-lanthana (CLA).

Some steps can be observed, which are crucial for better activity. As calcination temperature is increased, the lowest degree of aggregation is achieved with the alumina support which agreed well with the XRD results.

The XPS has been utilized to obtain information about the chemical composition of the outermost layers of the material. The core level spectra of the CLA sample calcined at various temperatures are shown in Fig. 3 and 4 corresponding to Ce 3d and O 1s, respectively. The La 3d and Al 2p core level spectra are presented in Fig. S2 (ESI†). The Ce 3d spectrum is composed of five spin-orbit doublets due to two multiplets, $3/2$ (u) and $5/2$ (v). Here, v/u , v^{II}/u^{II} , and v^{III}/u^{III} are attributed to Ce^{4+} : v/u and v^{II}/u^{II} are due to a mixture of $(5d\ 6s)^0 4f^2$ O $2p^4$ and $(5d\ 6s)^0 4f^1$ O $2p^5$ configurations, and v^{III}/u^{III} is due to the $(5d\ 6s)^0 4f^0$ O $2p^6$ final state. While, v_0/u_0 and v^I/u^I are due to $(5d\ 6s)^0 4f^2$ O $2p^5$ and $(5d\ 6s)^0 4f^1$ O $2p^6$ corresponding to Ce^{3+} .^{27,28} Generally, for alumina supported ceria systems, significant increase in the u_0/v_0 and u^I/v^I with simultaneous decrease in the u/v , u^{II}/v^{II} , and u^{III}/v^{III} peak intensities and hence an increase in the Ce^{3+} amount is noted (see Fig. S3, ESI†).²⁹ This interesting observation could be due to the perturbation of the electronic structure of the Ce ion brought out by a change in the coordination of the Ce and oxygen ligands when ceria is in contact with the alumina support.²⁹ However, for the CLA sample, as seen from the figure, with the alumina support and in turn with increase in the calcination temperature, no such increase (rather decrease) in the Ce^{3+} amount is observed. This observation revealed that the presence of La minimizes the interaction between Ce and Al which is

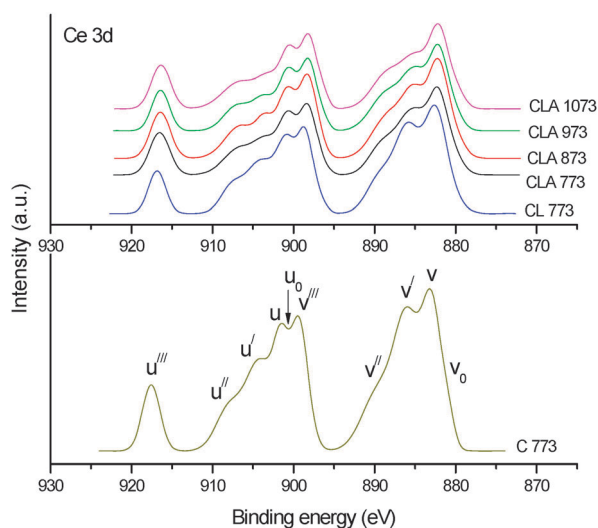


Fig. 3 Ce 3d XPS patterns of ceria (C 773), ceria-lanthana (CL 773), and alumina supported ceria-lanthana (CLA) calcined at various temperatures from 773 to 1073 K.

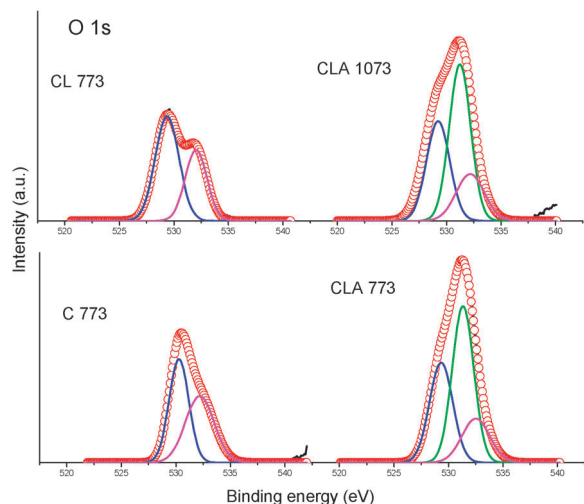


Fig. 4 Deconvoluted O 1s patterns of ceria (C 773), ceria-lanthana (CL 773), and alumina supported ceria-lanthana (CLA 773 and CLA 1073).

responsible for the formation of cerium aluminates, corroborating with the XRD results.

The O 1s XP spectra of CLA samples are shown in Fig. 4. For reference purpose, we have also included the XPS of ceria and CL samples. The core level peak of CLA is mainly composed of three characteristic component peaks. The component peak at a lower binding energy of $\sim 529.0 \pm 0.3$ eV is attributed to lattice oxygen of the rare-earth oxide.³⁰ Appearance of the peak at $\sim 531.0 \pm 0.3$ eV with an alumina support is due to the presence of Al-O characterized by an O 1s peak at this energy value. The peak at a high binding energy of $\sim 532.0 \pm 0.3$ eV corresponds to mixed contribution from carbonates, surface hydroxyl groups, and formation of $O^{\delta-}$ species at the surface. The hydroxyl groups are confirmed from the FTIR study (~ 3425 cm^{-1} ; OH stretching).^{30,31} Existence of more number of oxygen vacancies on the surface permits more amount of chemisorbed OH groups on the surface.

As calcination temperature increased, intensity of this particular peak is decreased due to removal of surface residues.

We have also calculated the atomic ratios at different calcination temperatures. With increase in the calcination temperature, an increase in the Ce/La (1.28 to 1.32) and Al/La (3.26 to 3.39) ratios is observed, which indicated a slight Ce enrichment and impediment of La over the surface. This could be due to alumina competing for the La as Ce does. As a consequence, La might irreversibly diffuse toward Al_2O_3 and simultaneously Ce reaches the surface to facilitate the La and Al interaction.³²

Raman spectroscopy provides information related to lattice oxygen vibrations. It is sensitive to the crystalline symmetry and, hence, a potential tool to obtain additional structural information. UV- and visible-RS of CL and CLA samples are presented in Fig. 5 and 6, respectively. UV-RS of pure ceria is also included in Fig. 5 for reference purpose. There are no peaks corresponding to Al_2O_3 in the case of CLA samples

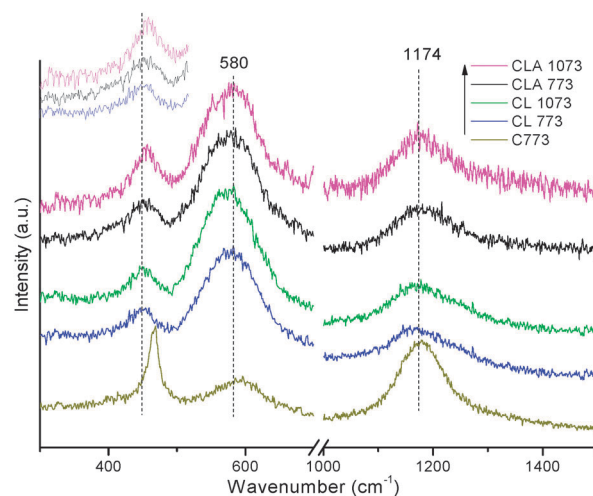


Fig. 5 UV-Raman spectra of ceria (C 773), ceria-lanthana (CL 773 and CL 1073), and alumina supported ceria-lanthana (CLA 773 and CLA 1073) (inset: expanded view of CL 773, CLA 773, and CLA 1073).

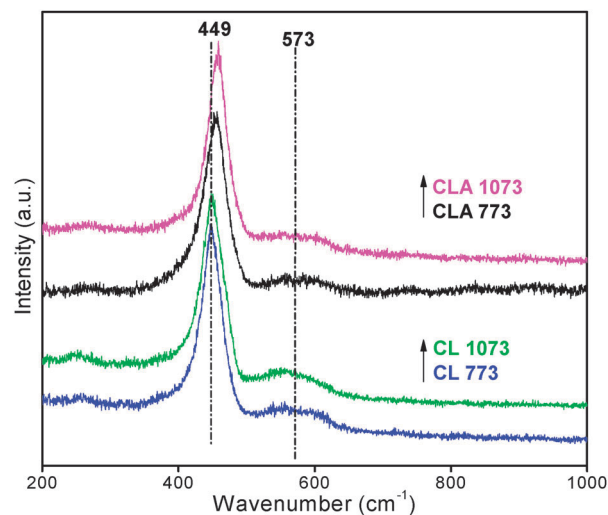


Fig. 6 Visible Raman spectra of ceria-lanthana (CL 773 and CL 1073) and alumina supported ceria-lanthana (CLA 773 and CLA 1073).

since $\gamma\text{-Al}_2\text{O}_3$ is Raman inactive in the investigated region ($100\text{--}1200\text{ cm}^{-1}$). There is one triply degenerate Raman active optical phonon located at 465 cm^{-1} , generally designated with F_{2g} symmetry, characteristic of fluorite-like structure, and can be viewed as symmetric breathing mode of the oxygen atoms around each cation.^{33–35} A significant decrease in the intensity and shift towards lower frequency is manifested as a result of asymmetry induced by randomly oriented oxygen vacancies (created during the partial incorporation of ceria by La). Besides this, two more bands are observed, one observed at $\sim 570\text{ cm}^{-1}$ is designated as the longitudinal optical (LO) band which allows this mode of vibration by relaxation of selection rules, is more defect sensitive, and relevant for the detection of O vacancies (from UV-RS, near surface oxygen vacancies while from visible-RS, bulk oxygen vacancies) created in the lattice cell that are known to facilitate the oxygen absorption and release from the surface.³⁵ For La doped ceria, substitution of every two La ions for Ce ions results in one oxygen vacancy leading to more defective material.³⁶ Hence, this band remarkably altered and became pronounced (particularly in UV-RS) for the doped ceria sample compared to pure ceria. This band position neither changed with the laser source nor with the dopant ion. The other second order LO band at $\sim 1170\text{ cm}^{-1}$ primarily corresponding to A_{1g} symmetry with small additional contributions from E_g and F_{2g} symmetries is also observed.^{5,34} This band is mainly observed in UV-RS. Similar to the 570 cm^{-1} band, the 1170 cm^{-1} band is also related to defects created in the lattice. The activation of these two LO bands is due to multi-phonon relaxation by the resonance Raman effect.³⁴ Corroborated with XRD results, cubic crystalline structure with oxygen vacancies is considered responsible for increase in the oxygen storage capacity (OSC) since these vacancies increase the bulk oxygen diffusion and thereby increase the ease with which the material can absorb and release oxygen that accounts for the OSC.

It is also noted from both UV- and visible-RS of CLA samples that there is a slight shift in the F_{2g} band position to higher wavenumber related to F_{2g} of CL which could be due to slight increment in the MO vibrations (see the inset of Fig. 5). The MO vibrations are rapid as soon as the large sized La^{3+} ions leave the ceria lattice. In addition, with increase in the calcination temperature the F_{2g} band intensity of UV-RS is slightly increased while the F_{2g} band of the visible-RS band remains unchanged.³⁷ It is well established that the UV-RS is surface sensitive, therefore the improvement in the F_{2g} band intensity may be due to the slight surface enrichment of Ce ions.^{38,39} Hence, the shift and high intensity of the F_{2g} peak also support the conclusions drawn from XRD and XPS.

From the UV-vis DRS measurements, information about the electronic states can be known. Deconvoluted UV-vis DRS of C 773, CLA 773, and CLA 1073 samples in the wavelength range $200\text{--}650\text{ nm}$ are presented in Fig. 7. The CLA samples exhibit three characteristic bands at ~ 255 , ~ 290 , and $\sim 346\text{ nm}$ corresponding to $\text{Ce}^{3+} \leftarrow \text{O}^{2-}$, $\text{Ce}^{4+} \leftarrow \text{O}^{2-}$, and interband transitions, respectively.¹⁷ The former band is slightly resolved compared to other two bands and observed due to defects created in the lattice during the dopant incorporation. The presence of this band justifies the Raman results. From UV-vis DRS measurements, we can also estimate the crystallite size

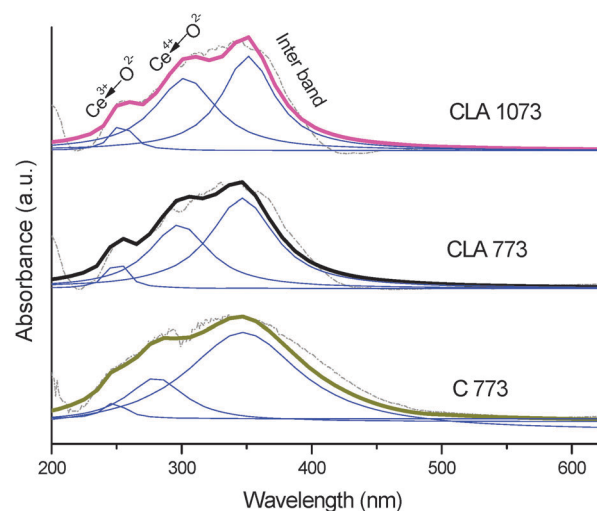


Fig. 7 UV-vis DRS of ceria (C 773) and alumina supported ceria-lanthana (CLA 773 and CLA 1073).

which could be explained on the basis of two facts. Considering quantum size effects, there is shifting of adsorption edge of CLA samples to higher energy level about $50\text{--}100\text{ nm}$ compared to ceria as a result of particle size decrease (related to interband transitions), on the other hand there are localized effects, arising from contributions of $\text{Ce}^{4+} \leftarrow \text{O}^{2-}$ charge transfer transitions for the small sized particles (a relatively broad band at $\sim 290\text{ nm}$).⁴⁰ The intensity of the interband transition increases with increase in the particle size accompanied by a decrease in the peak width. These results can further explain the crystallite growth with calcination temperature in line with XRD results.

H_2 -TPR profiles of CLA 773 and CLA 1073 samples are shown in Fig. 8. For reference purpose, the TPR of C 773 and CL (773 and 1073 K) samples are also included in the figure. The relative hydrogen consumptions calculated per gram of ceria for C, CL, and CLA calcined at 773 and 1073 K are presented in Table 1. Pure ceria has shown an extended peak at ~ 790 and another minor peak at $\sim 1059\text{ K}$ due to surface

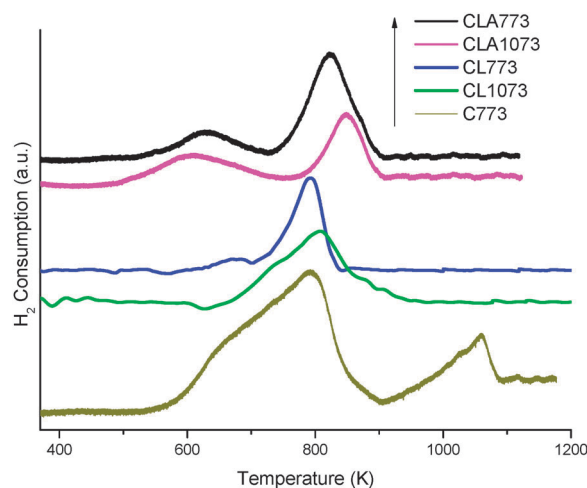


Fig. 8 TPR patterns of ceria (C 773), ceria-lanthana (CL 773 and CL 1073), and alumina supported ceria-lanthana (CLA 773 and CLA 1073).

and bulk reductions, respectively.³⁶ Unlike pure ceria, reduction of doped ceria is no longer confined to the surface but extends to the bulk. The observed peaks of CLA samples at 625 and 606 K are associated with the reduction of uppermost layers, and at 823 and 848 K are associated with the reduction of bulk for 773 and 1073 K, respectively. It is clear that the peaks of CLA samples shifted toward the lower temperature side in reference to pure ceria. Insertion of dopant ions induces distortion in the symmetry of the MO bond and results in highly mobile oxygen. Therefore, diffusion of this mobile oxygen through vacancies (created *via* charge neutralization) leads to an easy consumption of H₂. Generally, as calcination temperature is increased, the intensity of the reduction peak (surface as well as bulk) is expected to decrease and to shift to higher temperature due to sintering of the sample. It is interesting to note that the extent of surface reduction of CLA 1073 is increased instead and shifted to lower temperature compared to CLA 773, though the overall hydrogen consumption is decreased. If the surface area is solely influencing the redox nature then the surface reduction of CLA 1073 must be decreased which is not true. Hence, the reason for the shift in the surface reduction could be due to Ce surface enrichment (noted from XPS and RS). As calcination temperature is increased, an increase of reducible species (Ce) on the surface occurs, which eventually results in an increase in the surface reduction. In addition, generally for alumina supported ceria samples a significant peak is expected at *ca.* 1000 K temperature (Fig. S4, ESI†) attributed to the extent of interaction between Ce and Al characteristic of CeAlO₃ that shows a negative effect on the catalytic activity.⁴¹ In the investigated range, no such high temperature reduction peak is observed for the CLA sample. Therefore, combination of these two effects: shift and increase in the intensity of the low temperature peak (surface reduction) and the absence of a high temperature peak (~ 1000 K) evidences the inhibition of undesirable interaction between Ce and Al.^{41,42} Thus, in the presence of La, the redox properties of the ceria are greatly influenced.

3.2 Catalyst evaluation

Recently, Huang and Fabris investigated CO oxidation and proposed that the reaction proceeds *via* the Mars-van Krevelen reaction mechanism where CO adsorbs (through C-end) on the surface oxygen and simultaneously facilitates bond making between O of ceria and C of CO, and bond breaking between Ce–O, ultimately expelling the CO₂.⁴³ That means CO captures the oxide ions associated with the ceria and finally releases the CO₂ leaving an oxygen vacancy.^{44,45} This oxygen vacancy is replenished either by gaseous oxygen or by bulk oxygen. Therefore, reducible species that allow this vacancy creation and its replenishment limit the CO consumption. In this regard the activities of CL, CA, CZA, and CLA catalysts were evaluated based on the light-off temperature (T_{50} , where 50% of CO is consumed) and T_{100} .

Typical sigmoid curves obtained for CO conversion are presented in Fig. 9. The CO conversion over CZA and CLA samples calcined at 773 K is almost similar until the temperature reached 590 K and then the conversion on CLA increased steeply and reached 100% below 705 K, whereas on CZA, the

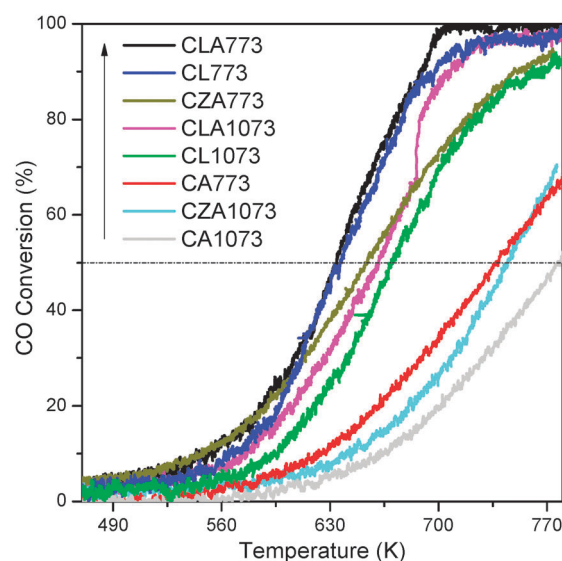


Fig. 9 Conversion of CO as a function of reaction temperature over ceria–lanthana (CL), alumina supported ceria (CA), alumina supported ceria–zirconia (CZA), and alumina supported ceria–lanthana (CLA) samples calcined at 773 and 1073 K (upward arrow indicates the decreasing order of T_{50}).

conversion increased aslant and reached a maximum of 93% at above 774 K. The T_{50} temperatures are around 633, 636, 653, 660, 670, 737, 744, and 778 K, respectively, for CLA 773, CL 773, CZA 773, CLA 1073, CL 1073, CA 773, CZA 1073, and CA 1073 samples. For both T_{50} and T_{100} , the CLA has shown better performance among the investigated samples.

A detailed discussion on synthesis and characterization pertaining to ceria–alumina (CA) and ceria–zirconia/alumina (CZA) samples can be found in our previous publications.^{9,11} The investigations on the CA sample revealed a steady decrease of the lattice parameter ($5.42 \rightarrow 5.39$ Å) with increasing calcination temperature, signifying the lattice contraction due to gradual insertion of Al³⁺ (0.051 nm) into the Ce⁴⁺ (0.097 nm) lattice. In the case of CZA, the Zr⁴⁺ (0.84 Å) dopant ion incorporation results in reduction in the lattice parameter (5.29 Å) compared to CeO₂ (5.41 Å) in agreement with Vegard's law. The crystallite size and surface area of CA and CZA materials are found to be 3.7 nm and 176 m² g^{−1} ceria, and 4 nm and 159 m² g^{−1} CZ, respectively. The crystallite size and surface area of both CA and CZA samples are better than that of the CLA sample while the amount of oxygen vacancies (confirmed from Raman) for the latter sample is predominately higher than the former.^{9,11} Although the aluminate formation is not seen from the XRD of CA and CZA,^{9,11} the relative stabilization of Ce³⁺ ions with alumina is observed from Ce 3d XPS (Fig. S3, ESI†, increased Ce³⁺ ions with alumina support) and is also verified from H₂-TPR (Fig. S4, ESI†, a significant reduction peak at the high temperature region), both these studies confirmed the weak interaction of Ce and Al.

The activity order is not consistent with the surface area order which clearly suggests that the surface area is not a major influencing factor for CO oxidation activity. Therefore, the high CO conversion for CLA 773 over CA 773 and CZA 773 samples could be attributed to various other factors such as increased reducibility, more number of oxygen vacancies,

and increased oxygen mobility in the defective structure as confirmed from the H₂-TPR, O 1s XPS, Raman results, and UV-vis DRS.^{9,11} The CO oxidation activity of CLA 1073 slightly decreased despite the available surface oxygen. Therefore, the bulk oxygen (observed from H₂-TPR) and its mobility appear to be the important factors for the genesis of CO oxidation activity. Further, the T_{50}/T_{100} difference (ΔT) between 773 and 1073 K calcined samples for CLA is small among the investigated samples which confers that the CLA sample is adequate to sustain the high degree of conversion. This incredible activity is attributed to involvement of an ample amount of reducible Ce ions due to the absence of undesired interaction between Ce and Al in the presence of La.

4. Conclusions

Alumina supported nanosized ceria–lanthana solid solutions were successfully synthesized by a deposition coprecipitation method from ultra high-dilute solutions using aqueous ammonia as the precipitating agent. It was confirmed from XRD, XPS, Raman, and H₂-TPR analyses that La³⁺ cations are involved in both the formation of Ce_{1-x}La_xO_{2-δ} solid solutions and the minimization of the undesired Ce and Al interaction. Smaller crystallites of the Ce–La solid solution over the alumina support are confirmed from XRD line broadening and suggested an excellent dispersion of the active phase over the support. The Raman and UV-vis DRS measurements revealed the presence of a larger number of oxygen vacancies in the Ce_{1-x}La_xO_{2-δ} solid solutions. The CLA sample exhibited a high CO oxidation activity and better thermal stability over CL, CZA, and CA samples. Thus, La³⁺ as a promoter has not only stifled the Ce–Al interaction but also enhanced the catalytic efficiency for CO oxidation.

Acknowledgements

L.K. and G.T. thank Council of Scientific and Industrial Research (CSIR), New Delhi, for senior research fellowships. Thanks are due to DST, New Delhi and DAAD, Germany, for financial support under a bilateral collaboration program (DST-DAAD-PPP-2010).

Notes and references

- H. Zhu, Z. Qin, W. Shan, W. Shen and J. Wang, *J. Catal.*, 2004, **225**, 267–277.
- N. R. E. Radwan, *Appl. Catal., A*, 2006, **299**, 103–121.
- B. Azambre, L. Zenboudj, A. Koch and J. V. Weber, *J. Phys. Chem. C*, 2009, **113**, 13287–13299.
- N. J. Castellani, M. M. Branda, K. M. Neyman and F. Illas, *J. Phys. Chem. C*, 2009, **113**, 4948–4954.
- W. Y. Hernandez, M. A. Centeno, F. Romero-Sarria and J. A. Odriozola, *J. Phys. Chem. C*, 2009, **113**, 5629–5635.
- W.-Q. Han, W. Wen, J. C. Hanson, X. Teng, N. Marinovic and J. A. Rodriguez, *J. Phys. Chem. C*, 2009, **113**, 21949–21955.
- B. Bonnetot, V. Rakic, T. Yuzhakova, C. Guimon and A. Auroux, *Chem. Mater.*, 2008, **20**, 1585–1596.
- A. B. Jorge, J. Fraxedas, A. Cantarero, A. J. Williams, J. Rodgers, J. P. Attfield and A. Fuertes, *Chem. Mater.*, 2008, **20**, 1682–1684.
- B. M. Reddy, P. Lakshmanan, P. Bharali, P. Saikia, G. Thirumurthulu, M. Muhler and W. Grünert, *J. Phys. Chem. C*, 2007, **111**, 10478–10483.
- M. L. Haro, K. Aboussaïd, J. C. Gonzalez, J. C. Hernández, J. M. Pintado, G. Blanco, J. J. Calvino, P. A. Midgley, P. B. Guillemaud and S. Trasobares, *Chem. Mater.*, 2009, **21**, 1035–1045.
- B. M. Reddy, K. N. Rao, G. K. Reddy, A. Khan and S.-E. Park, *J. Phys. Chem. C*, 2007, **111**, 18751–18758.
- S. Bernal, G. Blanco, G. A. Cifredo, J. J. Delgado, D. Finol, J. M. Gatica, J. M. R. Izquierdo and H. Vidal, *Chem. Mater.*, 2002, **14**, 844–850.
- R. D. Monte, P. Fornasiero, S. Desinan, J. Kaspar, J. M. Gatica, J. J. Calvino and E. Fonda, *Chem. Mater.*, 2004, **16**, 4273–4285.
- B. M. Reddy, P. Saikia, P. Bharali, S.-E. Park, M. Muhler and W. Grünert, *J. Phys. Chem. C*, 2009, **113**, 2452–2462.
- D. Gamarra, G. Munuera, A. B. Hungria, M. F. Garcia, J. C. Conesa, P. A. Midgley, X. Q. Wang, J. C. Hanson, J. A. Rodriguez and A. M. Arias, *J. Phys. Chem. C*, 2007, **111**, 11026–11038.
- J.-Y. Luo, M. Meng, Y.-Q. Zha and L.-H. Guo, *J. Phys. Chem. C*, 2008, **112**, 8694–8701.
- L. Katta, P. Sudarsanam, G. Thirumurthulu and B. M. Reddy, *Appl. Catal., B*, 2010, **101**, 101–108.
- F. Deganello and A. Martorana, *J. Solid State Chem.*, 2002, **163**, 527–533.
- R. K. Usmen, G. W. Graham, W. L. H. Watkins and R. W. McCabe, *Catal. Lett.*, 1995, **30**, 53–63.
- W. H. Cassinelli, L. S. F. Feio, J. C. S. Araujo, C. E. Hori, F. B. Noronha, C. M. P. Marques and J. M. C. Bueno, *Catal. Lett.*, 2008, **120**, 86–94.
- R. M. Navarro, M. C. Á. Galván, M. C. S. Sánchez, F. Rosa and J. L. G. Fierro, *Appl. Catal., B*, 2005, **55**, 229–307.
- R. Si, Y.-W. Zhang, S.-J. Li, B.-X. Lin and C.-H. Yan, *J. Phys. Chem. B*, 2004, **108**, 12481–12488.
- H. P. Klug and L. E. Alexander, in *X-ray Diffraction Procedures for Polycrystalline and Amorphous Materials*, John Wiley and Sons, New York, 2nd edn, 1974.
- A. B. López, I. S. Basáñez and C. S.-M. de Lecea, *J. Catal.*, 2006, **244**, 102–112.
- M. F. Wilkes, P. Hayden and A. K. Bhattacharya, *J. Catal.*, 2003, **219**, 305–309.
- F. Deganello, A. Longo and A. Martorana, *J. Solid State Chem.*, 2003, **175**, 289–298.
- P. Ji, J. Zhang, F. Chen and M. Anpo, *J. Phys. Chem. C*, 2008, **112**, 17809–17813.
- P. J. Miedziak, Z. T. Tang, T. E. Davies, D. I. Enache, J. K. Bartley, A. F. Carley, A. A. Herzing, C. J. Kiely, S. H. Taylor and G. J. Hutchings, *J. Mater. Chem.*, 2009, **19**, 8619–8627.
- P. J. Schmitz, R. K. Usmen, C. R. Peters, G. W. Graham and R. W. McCabe, *Appl. Surf. Sci.*, 1993, **72**, 181–187.
- Y.-W. Zhang, R. Si, C.-S. Liao and C.-H. Yan, *J. Phys. Chem. B*, 2003, **107**, 10159–10167.
- H. Borchert, Y. V. Frolova, V. V. Kaichev, I. P. Prosvirin, G. M. Alikina, A. I. Lukashevich, V. I. Zaikovskii, E. M. Moroz, S. N. Trukhan, V. P. Ivanov, E. A. Paukshtis, V. I. Bukhtiyarov and V. A. Sadykov, *J. Phys. Chem. B*, 2005, **109**, 5728–5738.
- D. H. Kim, S. I. Woo, J. M. Lee and O.-B. Yang, *Catal. Lett.*, 2000, **70**, 35–41.
- W. H. Weber, K. C. Hass and J. R. McBride, *Phys. Rev. B: Condens. Matter*, 1993, **48**, 178–185.
- T. Taniguchi, T. Watanabe, N. Sugiyama, A. K. Subramani, H. Wagata, N. Matsushita and M. Yoshimura, *J. Phys. Chem. C*, 2009, **113**, 19789–19793.
- F. J. P. Alonso, M. L. Granados, M. Ojeda, P. Terreros, S. Rojas, T. Herranz and J. L. G. Fierro, *Chem. Mater.*, 2005, **17**, 2329–2339.
- A. Trovarelli, *Comments Inorg. Chem.*, 1999, **20**, 263–284.
- M.-F. Luo, Z.-L. Yan, L.-Y. Jin and M. He, *J. Phys. Chem. B*, 2006, **110**, 13068–13071.
- W. Shan, Z. Feng, Z. Li, J. Zhang, W. Shen and C. Li, *J. Catal.*, 2004, **228**, 206–217.
- L. Dong, Y. Hu, M. Shen, T. Jin, J. Wang, W. Ding and Y. Chen, *Chem. Mater.*, 2001, **13**, 4227–4232.
- A. K. Sinha and K. Suzuki, *J. Phys. Chem. B*, 2005, **109**, 1708–1714.
- F. Yin, S. Ji, B. Chen, Z. Zhou, H. Liu and C. Li, *Appl. Catal., A*, 2006, **310**, 164–173.
- M. F. Garcia, A. M. Arias, A. I. Juez, C. Beller, A. B. Hungria, J. C. Conesa and J. Soria, *J. Catal.*, 2000, **194**, 385–392.
- M. Huang and S. Fabris, *J. Phys. Chem. C*, 2008, **112**, 8643–8648.
- M. Ozawa and C.-K. Loong, *Catal. Today*, 1999, **50**, 329–342.
- G. Balducci, M. S. Islam, J. Kaspar, P. Fornasiero and M. Graziani, *Chem. Mater.*, 2000, **12**, 677–681.